MAGNETOHYDRODYNAMICS Vol. 51 (2015), No. 4, pp. 721–747

MAGNETIC IRON OXIDE NANOPARTICLES AS MRI CONTRAST AGENTS – A COMPREHENSIVE PHYSICAL AND THEORETICAL STUDY

R. Taukulis[1,*], *M. Widdrat*[2,*], *M. Kumari*[3,*], *D. Heinke*[4,*], *M. Rumpler*[5,*], *É. Tompa*[6,*], *R. Uebe*[7,8,*], *A. Kraupner*[4], *A. Cēbers*[1], *D. Schüler*[7,8], *M. Pósfai*[6], *A.M. Hirt*[3], *D. Faivre*[2]

[1] *Institute of Physics University of Latvia, 8 Zeļļu, LV-1002 Rīga, Latvia*
[2] *Department of Biomaterials, Max Planck Institute of Colloids and Interfaces, Science Park Golm, 14424 Potsdam, Germany*
[3] *Institute of Geophysics, ETH-Zürich, Sonneggstrasse 5, CH-8092 Zürich, Switzerland*
[4] *nanoPET Pharma GmbH, Luisencarrée, RobertKochPlatz 4, 10115 Berlin, Germany*
[5] *Ludwig Boltzmann Institute of Osteology at the Hanusch Hospital of WGKK and AUVA Trauma Center Meidling, 1st Medical Department, Hanusch-Krankenhaus, Heinrich Collin Strasse 30, 1140 Vienna, Austria*
[6] *Department of Earth and Environmental Sciences, University of Pannonia, Egyetem u. 10, H8200 Veszprém, Hungary*
[7] *Ludwig-Maximilians-Universität München, Dept. Biologie I, Mikrobiologie, LMU Biozentrum, Großhaderner Str. 4, D-82152 Planegg Martinsried, Germany*
[8] *Universität Bayreuth, Dept. Microbiologie, Universitätsstraße 30, 95447 Bayreuth, Germany*
[*] *contributed equally to this work*
e-Mail: damien.faivre@mpikg.mpg.de

Magnetite nanoparticles, especially superparamagnetic iron oxide nanoparticles, are established contrast agents for magnetic resonance imaging. Magnetosomes, which are magnetite nanoparticles of biological origin, have been shown to have better contrast properties than current formulations possibly because of their larger size and high monodispersity. Here, we present an integrated study of magnetosomes and synthetic magnetite nanoparticles of varying size, hence, magnetic properties. We investigate not only the relaxation times as a measure for the contrast properties of these particles, but also their cytotoxicity and demonstrate the higher contrast of the larger particles. A theoretical model is presented that enables us to simulate the R_2/R_1 ratio of a contrast agent and confirm that larger particles offer higher contrast. The results from this study illustrate the possibility to obtain colloidal stability of large magnetic nanoparticles for magnetic resonance imaging applications and serve as an impetus for a more quantitative description of the contrast effect as a function of the size.

1. Introduction. The use of magnetic nanoparticles has developed into a major research area for bio- and nanotechnologists [1]. Translation to clinical studies has already started for magnetite nanoparticles in imaging studies among other application, due to their low toxicity and magnetic properties [2, 3]. Magnetic resonance imaging (MRI) is a particularly well-established diagnostic tool for obtaining images of any space in the human body. The main advantage of MRI is that it is harmless to the patient while delivering high resolution images of the body interior.

The magnetic properties of magnetite nanoparticles are dependent on their size. For equi-dimensional magnetite nanoparticles in the size range from 30 to 100 nm, the particles will be homogeneously magnetized, i.e. have one magnetic domain. This is referred to as stable single domain (SD) state and is defined by a high coercive force (H_c). Below 30 nm, the particles are in the superparamagnetic (SP) state. These are also SD, but the anisotropy energy is sufficiently low com-

pared to thermal energy for flipping the magnetic moment of the particle at the timescale of observation. SP magnetite saturates quickly in fields $< 150\,\mathrm{mT}$ and has no coercivity.

Contrast enhancement in MRI is achieved by changing the magnetic relaxation times T_1 and T_2 of the hydrogen protons contained in the tissue. For MRI, two different classes of contrast agents exist: agents that influence mainly the signal in T_{2-} (i.e. negative contrast agents, reducing the signal) or T_{1-} weighted images (i.e. positive contrast agents, increasing the signal). The degree of the T_2 contrast effect is typically represented by the spin-spin relaxivity $R_2 = 1/T_2$, where higher values of R_2 result in a larger contrast effect. Because R_2 is strongly related to μ, the magnetic moment of the contrasting nanoparticles, which in turn is dependent on the size as seen above, it is not surprising that larger particles should provide enhanced properties as contrast agents relative to smaller ones [4, 5]. However, an experimental proof obtained on particles of similar batches is lacking as well as the related theoretical description relating the contrast properties to the particle size.

SPION (superparamagnetic iron oxide nanoparticles) combine a magnetic core with a coating agent that is an approved pharmaceutic for contrast agent use in MRI. Although commercial formulations are already on the market (e.g., Ferumoxtran for lymph node diagnosis, Feridex or Resovist for liver diagnosis) [2, 6], none uses biogenic magnetite. SPION are smaller than magnetosomes and by far less monodisperse than the biological magnetite [7]. Therefore, magnetosomes potentially provide better contrast properties for MRI. Their potential for MRI has been recognized because they have been shown to possess an even larger R_2/R_1 ratio than commercially available contrast agents [8]. However, it is currently not possible to form magnetosomes in amounts required for pharmaceutical applications and their cytotoxicity remains to be fully characterized.

We have recently shown that the particle size of magnetite nanoparticles can be controlled in aqueous-based processes [9] and that particles of dimensions similar to those of bacterial magnetosomes can be obtained by this process [10]. In addition, we have also demonstrated that the dimension of the magnetosome particles can also be controlled, in this case by genetic engineering [11–13]. Here, we thus present an integrated study comparing the structural and magnetic properties of magnetite nanoparticles. We assess their potential as a contrast agent for MRI by testing not only their relaxation times but also their biocompatibility. In particular, we test if the high contrast properties obtained for magnetosomes are only due to their size or if further properties, such as monodispersity or colloidal stability, are at the origin of this remarkable feature. In addition, we present a method to calculate the relaxivity of magnetic nanoparticles in MRI. This quantitative description of the relationship between contrast properties and particle size confirms the results we obtained experimentally and can be used to assess the theoretical potential of other particles.

2. Results and discussion. The main findings from this study can be illustrated from the results of five biogenic and six synthetic samples (Table 1). The samples are categorized as small biogenic (SB), large biogenic (LB), small inorganic (SI) and large inorganic (LI).

2.1. Structure, size and morphology of the nanoparticles. All samples consist of nanoparticles of pure magnetite, as indicated by the observed peaks in the X-ray diffractogram (Fig. 1) and by diffraction maxima measured in SAED patterns (Fig. 2*c*,*d*).

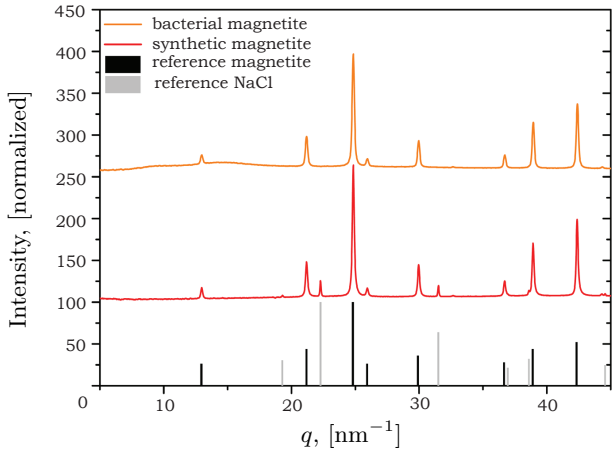

Fig. 1. X-ray diagram of representative bacteria (LB3 3, orange) and synthetic (LI 2, red) samples as well as reference materials. The salt peak (NaCl) originates from the drying of the samples and is due to the fact that FeCl and NaOH are used in the magnetite synthesis.

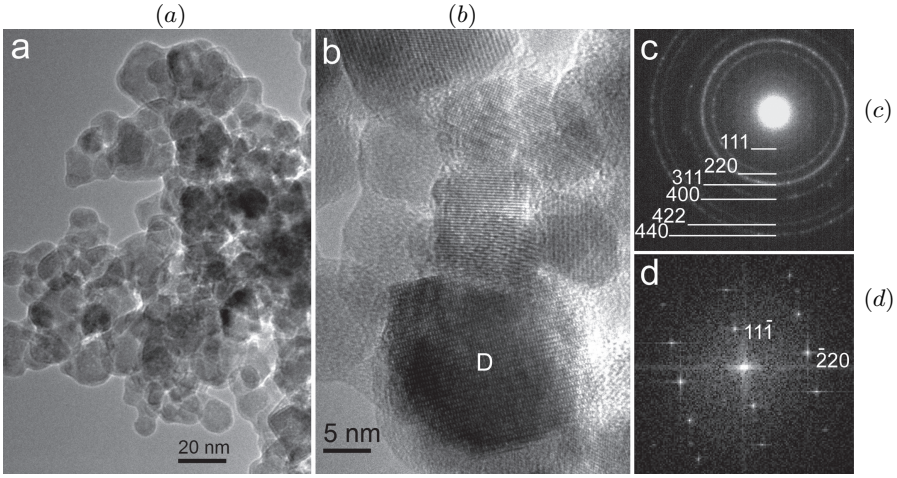

Fig. 2. (*a*) A typical view of magnetite nanoparticles in SI1. (*b*) A HRTEM image of several nanoparticles, showing euhedral shapes and perfect crystalline structures. (*c*) A SAED pattern obtained from a cluster of nanoparticles, and (*d*) a Fourier transform of the HRTEM image of particle D in (*b*). Both the ring pattern in (*c*) and the intensity maxima in (*d*) can be indexed according to the structure of magnetite.

2.1.1. Synthetic samples. The size of the individual nanoparticles ranges from a few to several tens of nanometers (Table 1). The mean sizes determined by TEM for the particles in the SI samples are in good agreement with the sizes obtained using synchrotron X-ray diffraction. The size of larger particles (LI samples) is difficult to determine from TEM micrographs because of aggregation.

All synthetic samples are very similar in that they contain clusters of nanoparticles in random orientations (Fig. 2*a*), with most particles having euhedral (octahedral or cuboctahedral) shapes and typically perfect structures (Fig. 2*b*), as suggested by high-resolution TEM images. SAED patterns obtained from both clusters of crystals (cf. ring patterns in Fig. 2*c*) and from individual nanoparticles are consistent with the structure of defect-free magnetite (Fig. 2*d*).

Table 1. Summary of the properties of the nanoparticles. Acronyms used for a samples names: SB stands for Small and Biological, LB for Large and Biological, SI for Small and Inorganic, LI for Large and Inorganic, S for Stabilized. d_c , d_h are the core and the hydrodynamic diameter, respectively. M_{rs}/M_s and H_{cr}/H_c are the magnetic properties described in the chapter on magnetic properties; the following six columns depict the biocompatibility properties of the samples. The final three columns depict the MRI contrast properties of the samples. IGC50: concentration at which the growth of cells is inhibited by 50%.

Sample description	d_c [nm]	d_h [nm]	Stab. agent	$\frac{M_{rs}}{M_s}$	$\frac{H_{cr}}{H_c}$	EZ4U NIH3T3 [IGC50, mg/ml]	EZ4U RAW264.7 [IGC50, mg/ml]	EZ4U MC3T3-E1 [IGC50, mg/ml]	LDH NIH3T3 [IGC50, mg/ml]	LDH RAW264.7 [IGC50, mg/ml]	LDH MC3T3-E1 [IGC50, mg/ml]	R_1 [L/mmol·s]	R_2 [L/mmol·s]	$\frac{R_2}{R_1}$
SB1	24	90		0.05	N/A							9.0	320.7	35.6
LB1	41	143		0.38	1.5							8.6	541.5	63.1
LB2	38	84		0.38	1.3	0.94	0.05	0.13	0.82	0.07	0.12	8.8	477.1	54.2
SB2	29	76		0.20	2.8	0.72	0.18	0.12	0.54	0.16	0.12	11.0	442.5	40.1
LB3	32			0.25	1.4	0.68	0.19	0.13	0.48	0.43	0.12			
LI1s	28	115	DOPA	0.20	1.78							12.1	330.1	27.1
LI2	36			0.22	1.57	0.34	0.29	0.65	0.27	0.37	0.53			
LI3	33			0.20	1.60	0.50	0.23	0.65	0.44	0.22	0.53			
LI4	26.5			0.21	1.65	0.31	0.48	0.49	0.22	0.65	0.20			
SI1	17			0.06	2.25	0.52	0.15	0.58	0.48	0.55	0.33			
SI1s	17	123	DOPA									14.9	244.5	16.4
SI2	18			0.09	2.46	0.53	0.24	0.45	0.49	0.55	0.20			
SI2s	18	100	DOPA	0.01	0							15.3	302.6	19.7
Resovist	5	63		0.01	0	0.16						20.0	219.3	11.0

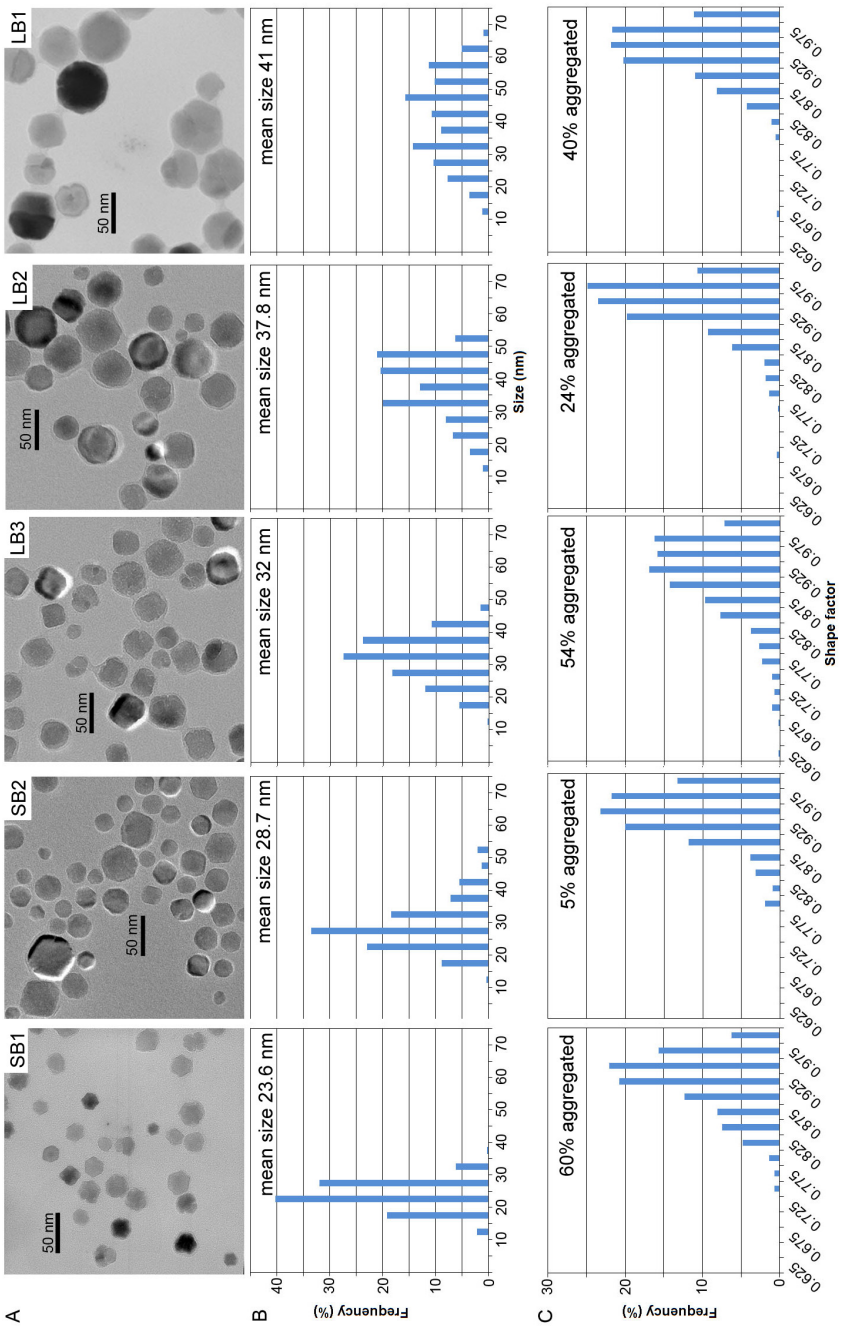

Fig. 3. (*a*) Bright-field TEM images of typical magnetite magnetosomes from five different bacterial samples, with the sample identifiers indicated on the top (cf. Table 1). (*b*) Particle size distributions as measured from TEM micrographs. (*c*) Shape factor (width/length) distributions of particles in the same samples, with the fraction of twinned or aggregated particles indicated in each panel.

The particle size distribution of SI1 has a maximum at 15 nm, but extends to approximately 30 nm (Supplementary Fig. 1), LI2 and LI3 also consist of mostly small (∼15 nm) magnetite nanoparticles; however, these samples also contain larger aggregates that apparently formed from randomly or similarly oriented nanocrystals.

2.1.2. Biological samples. In all biological samples, the magnetosomes extracted from different strains of the magnetotactic bacterium *Magnetospirillum gryphiswaldense* (Table S1) are still enveloped by the magnetosome membrane. This surface layer prevents clustering/aggregation of the particles and results in a dispersed distribution of magnetosomes on the TEM grid. Typically, particles larger than 30 nm in diameter form chains, whereas smaller particles appear randomly scattered (Fig. 3).

Compared to magnetosomes of the wild-type, particles of mutant strains (LB2) show a difference in both particle size and shape. This mutation is not expected to alter the physico chemical properties of the particles except their size and shape. Whereas the wild-type particles produce a negatively-skewed size distribution, size distributions in mutant samples are lognormal-like (SB2), Gaussian (SB1 and LB3) or broad, double-peaked (LB1) (Fig. 3*b*). The mean size of the distributions increases from 23.6 nm (SB1) to 41 nm (LB1). Concerning the shapes of the particles, samples LB2 and SB2 contain wild-type-like, mostly single crystalline, euhedral particles (Fig. 4*a*).

The shape factor distribution is relatively narrow in these samples and resembles the curves that are typically obtained for magnetosomes from the wild-type (Fig. 3*c*). In the other samples, however, a large fraction of the magnetosomes is either twinned or multiply aggregated. This effect is most pronounced in the case of SB2 which contains relatively large crystals, most of which are composed of several crystallites (Fig. 4*b*). The aggregated nature of the magnetosomes clearly affects their shape factor distribution because samples containing a large fraction of twinned or aggregated particles produce broad shape distributions (Fig. 3*c*). The TEM-based particle size and shape measurements are entirely consistent with the bulk magnetic data as shown below.

2.2. Magnetic properties. Biological samples show a large variation in their magnetic properties (Table 1). SB1 has a closed hysteresis loop, which would be

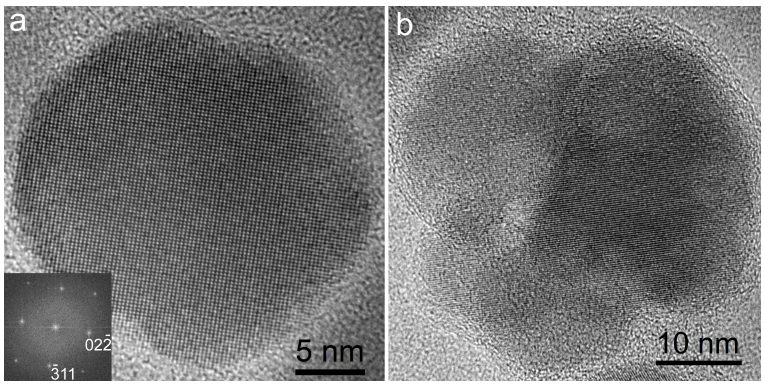

Fig. 4. HRTEM images of (*a*) a single-crystal magnetosome with a perfect structure from SB2, with the Fourier transform of the image in the lower left, indicating that the crystal is viewed along the [223] crystallographic direction, and (*b*) an aggregate magnetosome that consists of at least three individual crystals, from sample LB3.

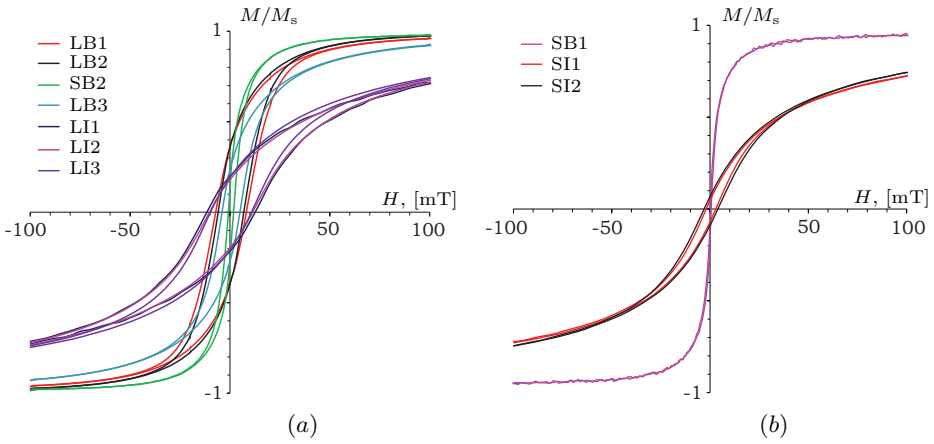

Fig. 5. Normalized hysteresis loops for chemically synthesized and biologically mineralized magnetite nanoparticles with the average particle size in the (*a*) SSD and (*b*) SP domain.

expected for true SP behavior (Fig. 5). The hysteresis loops of the other biological samples are open, and the ratios of remanent saturation magnetization to saturation magnetization ($M_{\mathrm{rs}}/M_{\mathrm{s}}$) and remanent coercivity to coercivity ($H_{\mathrm{cr}}/H_{\mathrm{c}}$) are compatible with a mixture of SD and SP particle sizes. All synthetic samples show an open hysteresis loop (Fig. 5). The magnetization ratio is variable and suggests a SD particle size with a significant SP contribution. The approach to saturation magnetization of synthetic particles is slower (low susceptibility) and requires much higher fields to reach saturation if compared to biological particles.

First order reversal curve (FORC) analysis is a powerful technique for characterizing ferromagnetic minerals (s.l.), their domain state (SP and SD), and the extent of interactions between particles [14–17]. FORC distributions located near the origin, i.e. at the cross-section of the interaction axis (H_{b}) and the coercivity axis (H_{a}), with an upward offset signify non-interacting particles, whereas a spread along H_{a} signifies a distribution in particle size. A spread along H_{b} on the FORC diagram indicates the presence of interacting SD particles. FORC diagrams for SB1, SB2, SI1, and SI2 reveal the dominance of magnetite nanoparticles that are SP (Fig. 6). The other samples contain a broader mixture of SP and SD particle sizes.

Decomposing the FORC measurements into the reversible and irreversible parts of the induced magnetization clearly shows the relative magnitudes of the SP and SD contributions (Fig. 7) [18]. Samples LB1, LB2, LI2, LI3, and LI4 have a larger contribution of irreversible magnetization, i.e. the SD particle size. LB3 has less of the contribution from SD particles, and samples SB2, SI1 and SI2 are largely SP. Only SB1 is almost purely SP in its magnetic behavior.

From FORC analysis one sees that the biological SD samples exhibit a lower spread on the H_{b} (interaction) axis, varying between $\pm 15\,\mathrm{mT}$, if compared to the synthetic samples that range from $-30\,\mathrm{mT}$ to $+40\,\mathrm{mT}$. This suggests a lower degree of the interaction among magnetite particles from biologic origin if compared to chemically synthesized ones. There is also a larger spread in coercivity distribution of the synthetic samples, e.g., it ranges from $0\,\mathrm{mT}$ to $40\,\mathrm{mT}$ for SI1 with the smallest particle size distribution if compared to SB1. It should be noted that the larger degree of interactions in the synthetic samples may lead to a larger effective magnetic particle size in comparison to their physical size, i.e. aggregates

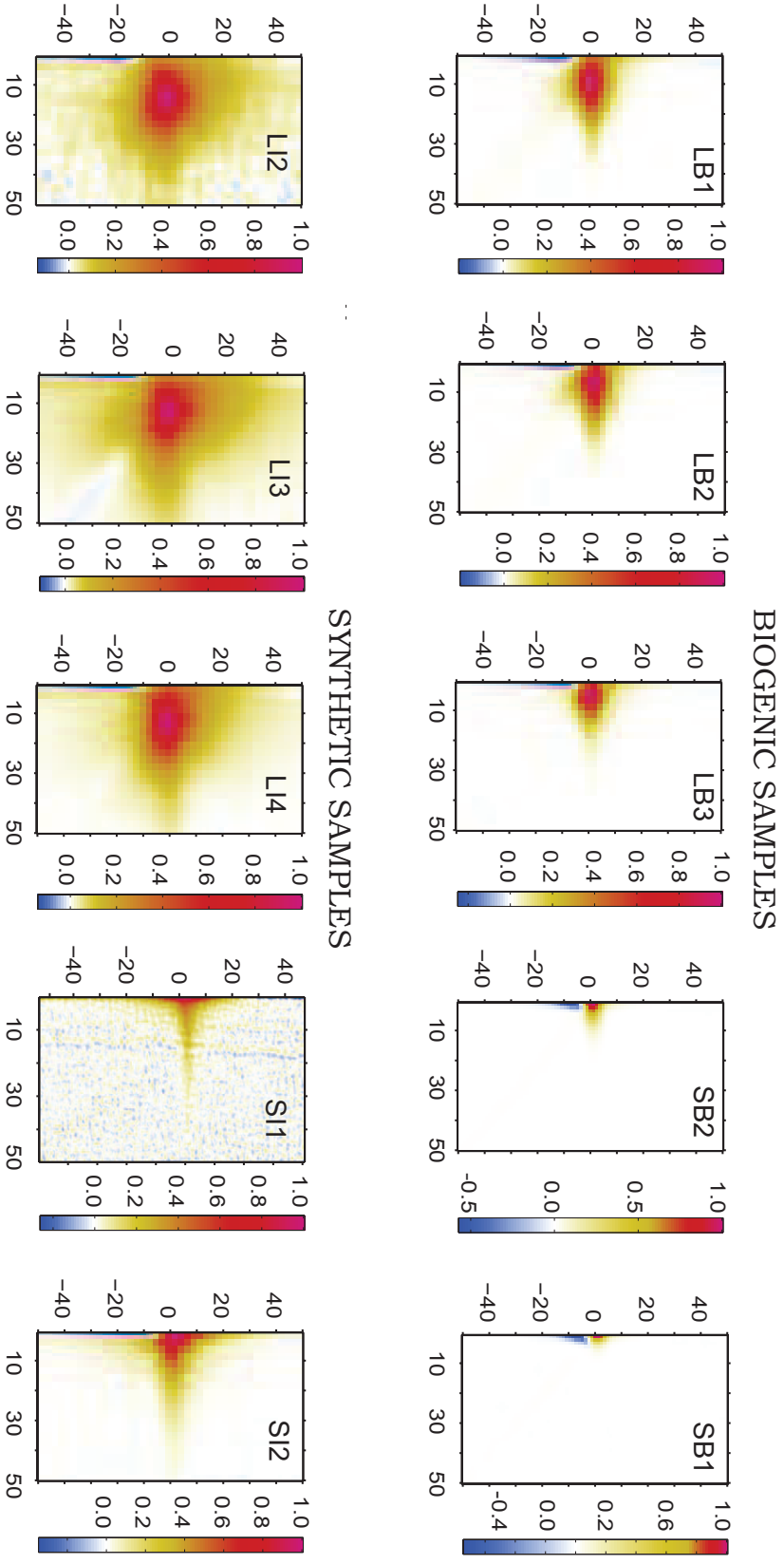

Fig. 6. FORC diagrams for biogenic and synthetic magnetite nanoparticles. The smoothing factor is 2.

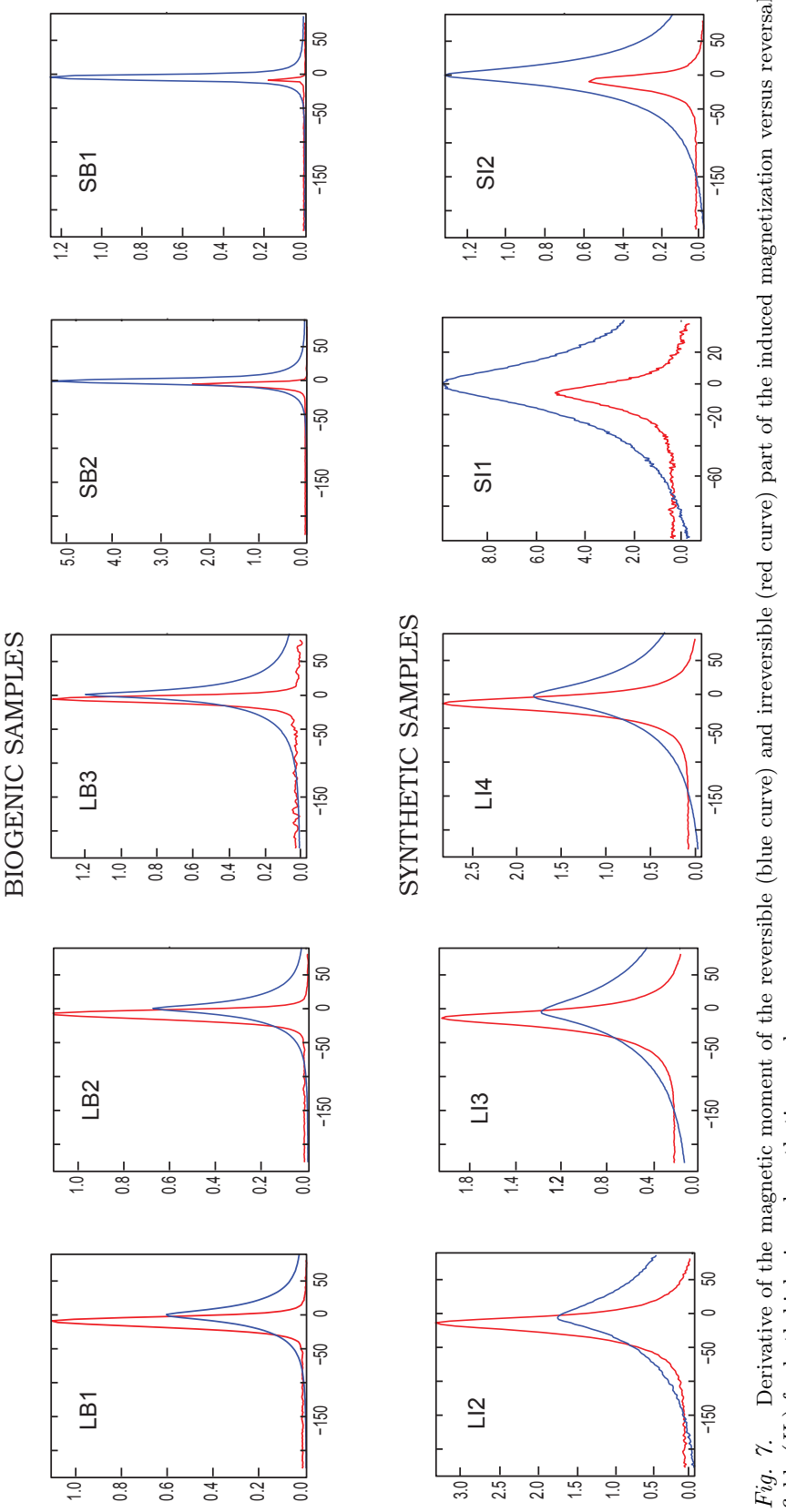

Fig. 7. Derivative of the magnetic moment of the reversible (blue curve) and irreversible (red curve) part of the induced magnetization versus reversal fields (H_r) for both biologic and synthetic samples.

of SP particles behave like the SD size. Afterward SI1 was coated with L-3,4 Dihydroxyphenylalanin (L-DOPA) (SI1s) which inhibited the particle interaction. The FORC distribution is concentrated at the origin, as would be expected for purely SP particles, and the magnetization is largely reversible (Supplementary Fig. 2), similar to what is found for SB1. Resovist shows a largely reversible magnetization similar to what is seen in SI1s and SB1 (Supplementary Fig. 3). Truncating the FORC distribution to suppress the very low coercivity, however, shows that there are particles with a higher coercivity (cf. inset Supplementary Fig. 3). This higher coercivity tail is not found in SB1 and SI1s.

In summary, FORC analysis demonstrates that the magnetic properties of samples SB1, SB2, SI1 and SI2 are dominated by the SP fraction in the sample. Samples LB1, LB2, LB3, LI2, LI4 and LI4 may also have SP particles, but the SSD particles dominate. Coating the synthetic particles is successful in breaking down the particle interaction, so that their magnetic properties are SP.

2.2.1. Biocompatibility. The biocompatibility of the synthetic and biological samples was tested by different assay systems: EZ4U and LDH assays, using various cell lines: MC3T3-E1 osteoblast, NIH3T3 fibroblasts and RAW264.7 macrophages (Table 1). IGC50 values obtained by the EZ4U and LDH assays give similar results for all synthetic and biological samples within one cell line. More specifically, IGC50 values of the synthetic particles, which were determined in the three cell lines, range from 0.15 – 0.65 mg/ml in the case of EZ4U assay and between 0.20 – 0.65 mg/ml in the case of LDH assay. These results demonstrate that IGC50 values of the synthetic particles with sizes between 17 – 36 nm do not depend on the size.

The biocompatibility of numerous types of artificially synthesized nanoparticles, e.g., chitosan, silica and zinc oxide, has been determined using various cell lines [19 – 22]. IGC50 values of 0.1 – 0.25 mg/ml were reported for iron oxide nanoparticles [23, 24]. The IGC50 values from this study are not broader and only slightly higher than values reported in these investigations and show that the cytotoxicity of our synthetic inorganic iron oxide particles is comparable to synthetic particles from, e.g., chitosan or zinc oxide.

The IGC50 values of the biological particles show a larger variation than those of synthetic particles. They are, however, similar within one cell line. IGC50 values evaluated by EZ4U and LHD assays in MC3T3-E1 and RAW264.7 cells range from 0.05 to0.19 mg/ml and 0.07 to0.43 mg/ml, respectively. In NIH3T3 cells, IGC50 values are higher than in the other two cell lines, which cannot be explained at present. IGC50 value in NIH3T3 cells, determined by EZ4U and LDH assays, range from 0.48 to 0.94 mg/ml. Thus, the applied genetic manipulation of the biological nanoparticles did have an effect on the IGC50 values in the tested cell lines. In general, the synthetic particles are less toxic to the cells than the biological ones, probably due to the presence of remaining bacterial cell components on the magnetosome membrane.

2.3. Colloidal stability. The biological samples were found to be colloidally stable without further stabilization. This behavior can be attributed to the magnetosome's membrane, which is sufficient to stabilize the particles in aqueous media. The synthetic particles, on the other hand, specifically those exhibiting large crystal sizes and hence high magnetic attraction forces, are prone to aggregation. Thus, stabilization is essential for these nanoparticles because a surface modification during the synthesis step is missing.

Particles can typically be colloidally stabilized using two different approaches: electrostatic or steric stabilization. Iron oxide nanoparticles for biomedical applications are typically sterically stabilized by using biocompatible dispersants, such

as dextran [25], polyethylene glycol [26] or poly (vinyl alcohol) [6]. These dispersants are physically adsorbed on the particle surface and prevent the particles from aggregation due to steric repulsion. Because non-ionic stabilization polymers do not lead to any colloidally stable dispersion, cationic polymers, such as polyethylenimine (PEI) and chitosan, were found to be good dispersants for the synthetic particles (data not shown). PEI and chitosan are known to offer an exceptionally strong adhesion because of additional ionic interactions with the particle surface [27]. Electrostatic stabilization, in turn, can be achieved by introducing an anionic/cationic charge [6] either due to anions/cations or due to monomers with a charged functional group, i.e. citric acid [28]. The most promising results were obtained using L-DOPA, which is known to exhibit high affinity anchor groups for iron oxide particles that leads to highly stable dispersions [29].

The stabilization of the synthetic particles LI1, SI1, and SI2 was successful, and the stabilized dispersion of SI2s using L-DOPA is exemplary shown in Fig. 8. The change in colloidal stability can be clearly visually observed and is also reflected by the hydrodynamic diameter which is in the range of 100 – 125 nm after the stabilization. The stabilized particles show good colloidal stability until present, six months after treatment. Stabilization of the samples LI2, LI3 and LI4 was not successful. This can be attributed to the larger core sizes which lead to stronger magnetic interaction (i.e. larger contribution of irreversible magnetization, cf. Fig. 7), which results in irreversible aggregation.

2.4. MRI relaxivity. In general, paramagnetic and superparamagnetic substances lead to a shortening of the relaxation times T_1 (spin–lattice relaxation time) and T_2 (spin-spin relaxation time) of the hydrogen protons in the surrounding tis-

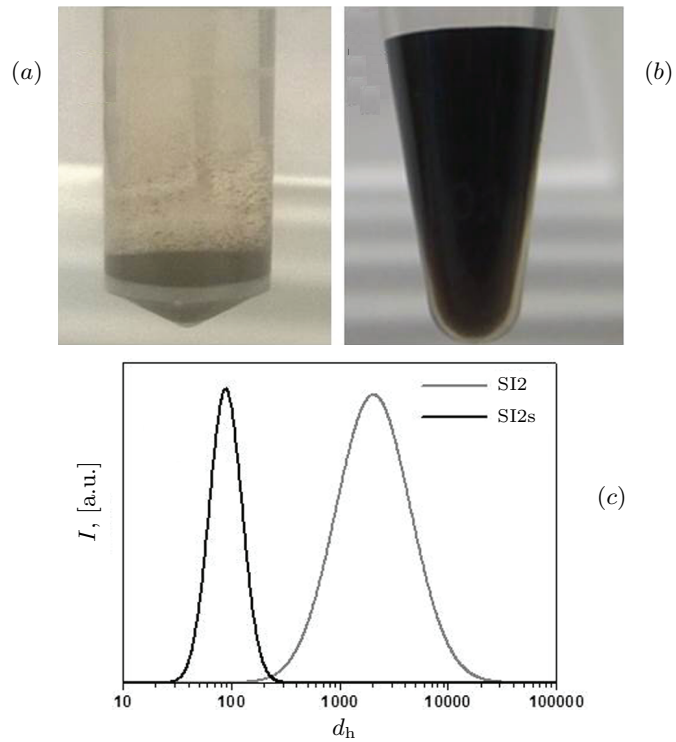

Fig. 8. Sample SI2 (*a*) before and (*b*) after stabilization using L-DOPA. The log-normal distribution of the hydrodynamic diameter (*c*) of the original and stabilized particles clearly indicates the stabilization effect.

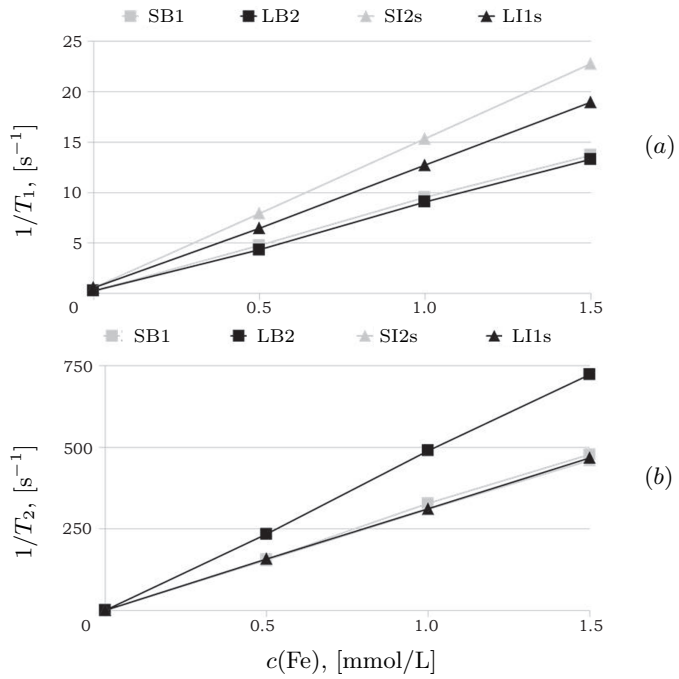

Fig. 9. Concentration dependent relaxation rates (*a*) $1/T_1$ (R_1) and (*b*) $1/T_2$ (R_2) determined at 0.94 T and 39°C. Biological particles are represented by squares and synthetic particles are represented by triangles, respectively.

sue. Iron oxide nanoparticles exhibit an especially strong shortening of T_2, for which they are also called T_2-contrast agents. The higher the shortening of T_2, which is equivalent to a high R_2 relaxivity, the higher the obtained T_2 weighted contrast. Contrast agents, in general, are characterized by the ratio of the relaxivity R_2/R_1. Therefore, a high T_2 weighted contrast can be obtained by combining high R_2 values with low R_1 values. In order to investigate the potential suitability of the particles as contrast agents in MRI, the relaxation times were measured and compared with the known contrast agent Resovist.

Fig. 9 illustrates the relationship between the relaxation rates $1/T_1$ and $1/T_2$ and iron concentration. As expected, both relaxation rates increase with increasing iron concentration. The relaxation rates of all particles show good linearity in the measured concentration range, which is an indication for non-interacting particles and colloidal stability. Colloidal stability is mandatory for the determination of the relaxivity values R_1, R_2 and R_2/R_1.

The dependence of the relaxivity on the core diameter d_c of different particles is shown in Fig. 10. Independent of the origin of the particles, biological or synthetic, the R_2 relaxivity increases roughly linearly with the core diameter d_c. The increase of the R_2 relaxivity with the particle size can be explained by the fact that larger particles exhibit stronger magnetic moments, which leads to a faster dephasing of the hydrogen protons and, therefore, to a stronger shortening of T_2. It is known that the T_2-effect dominates for iron oxide particles over the T_1-effect. We also observe a slight dependence of R_1 on the size: a decreasing T_1 effect is obtained for increasing core diameter. Considering the R_1 and R_2 relaxivities, the decisive R_2/R_1 ratio increases with the core diameter.

It has to be noted that in addition to the dependence of the relaxation properties on the core diameter d_c, a strong dependence was also found on the hy-

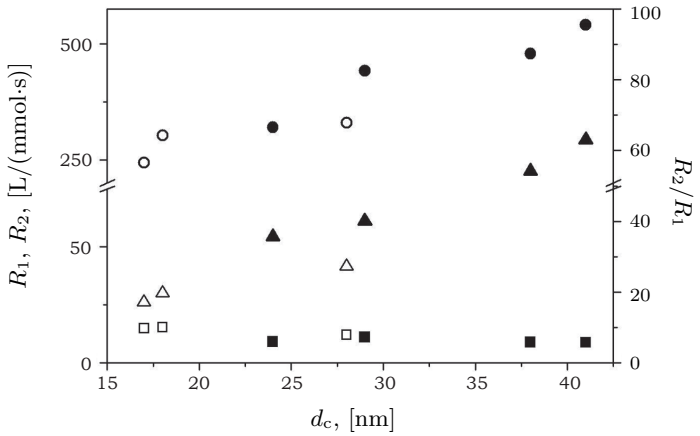

Fig. 10. Size dependence (d_c) of the R_1 relaxivity (square), R_2 relaxivity (circle) and the ratio R_2/R_1 (triangle). Biological particles are represented by filled symbols and synthetic particles are represented by blank symbols, respectively.

drodynamic diameter d_h (data not shown). Therefore, only particles with similar hydrodynamic diameters can be compared directly (see Table 1).

The biological particles were measured in the original state because of their sufficient colloidal stability. Compared to Resovist, the smallest biological particles SB1 ($d_c = 24$ nm) exhibit a 1.5-fold increase in R_2 and a 3.2-fold increase in R_2/R_1. In accordance with the observed size-dependence, the large biological particles LB2 ($d_c = 38$ nm) show an improved relaxation behavior with a 2.2 fold higher R_2 relaxivity and, due to the low R_1 relaxivity, even a 4.9-fold higher R_2/R_1 relaxivity.

The relaxation properties of the original synthetic particles could not be measured because of colloidal instability; therefore, only the L-DOPA-stabilized particles were used for the determination of the relaxation properties. The R_2 relaxivity is increased compared to that of Resovist, but, due to the overall smaller core diameters, only to a limited degree. The SI2s particles with the smallest core diameter ($d_c = 18$ nm) showed a 1.4-fold increase in R_2 and a 1.8-fold increase in R_2/R_1. The observed size dependence also applies to the synthetic particles, where the sample LI1s with a larger core diameter ($d_c = 28$ nm) showed enhanced relaxation effects. Accordingly, LI1s provided a 2.5-fold increase of R_2/R_1 compared to Resovist.

This study was focused on the determination of the MRI relaxation times and showed the advantage of larger particles in T_2-weighted imaging. Besides the relaxation times, for a successful use of the particles *in vivo* and for an extensive description of the contrast properties, aspects like blood half-life, biodistribution, clearance properties and particle surface characteristics, are all expected to play an important role. The blood half-life is closely connected with the uptake process into the mononuclear phagocyte system (MPS) and is faster for larger particles. [30, 31] For this reason, the larger particles may not be perfectly suited, despite the best relaxation properties, the particles may not be perfectly suited in applications where a long blood half-life is needed (e.g., angiography). In this case, smaller particles with less enhanced relaxation properties are preferred. On the other hand, the large particles can be used for applications where a fast uptake by the macrophages (MPS) is preferred, e.g., liver/spleen imaging or macrophage associated inflammation imaging [32, 33]. In addition, different surface coatings of the biological and synthetic particles (magnetosome membrane vs. L-DOPA

coating) may influence the blood kinetics and affect the *in vivo* behavior of the particles [34]. These examples show that not only the relaxation properties of the particles are decisive for a new MRI imaging agent, but also aspects concerning the particle behavior *in vivo* have to be taken into account. An extensive *in vivo* characterization of the particles investigated in this study will be the subject of a future work.

2.5. Simulation of contrast properties. In order to better understand factors that affect relaxivity in a particle system, a model has been developed to calculate changes in relaxivity by varying different physical parameters, such as the core and hydrodynamic diameters, the particles magnetization and its anisotropy, external field strength, or the ratio between "inner" and "outer" viscosities. Expressions for the longitudinal T_1 and transversal T_2 relaxation times of protons are derived from a semi-classical model, where the protons are described in the frame of quantum mechanics, and magnetic nanoparticles are treated classically as macroscopic objects. Magnetic nanoparticles create random magnetic fields acting on the protons. Their randomness originates first from the distance between the nanoparticle and the proton, which is random due to thermal diffusion of water molecules, and second due to thermal fluctuations of the magnetic moment of the particle. As a result, the longitudinal and transversal relaxation times of the proton are expressed through time correlation functions of the magnetic moment of the nanoparticle and through the function j [35] describing the thermal motion of the proton in the vicinity of the nanoparticle.

Time correlation functions of the magnetic moment are calculated using the "egg-yolk" model [36], which takes into account the simultaneous Brownian rotation of the particle ("egg") and the magnetic moment ("yolk"). The model accepts three non-dimensional parameters corresponding to external field strength, anisotropy of the particle, and ratio of "inner" and "outer" viscosities of the particle. These parameters can be calculated from the physical parameters of the system as follows:

$$\xi = \frac{\mu H}{k_{\mathrm{B}} T}; \quad \sigma = \frac{K V_{\mathrm{m}}}{k_{\mathrm{B}} T}; \quad \epsilon = \frac{\tau_{\mathrm{m}}}{\tau_{\mathrm{B}}},$$

where μ is the magnetic moment of the particle, H the external magnetic field, k_{B} the Boltzmann constant, T the temperature, K the magnetic anisotropy constant of the particle, V_{m} the magnetic volume of the particle, and τ_{m} and τ_{B} the char-

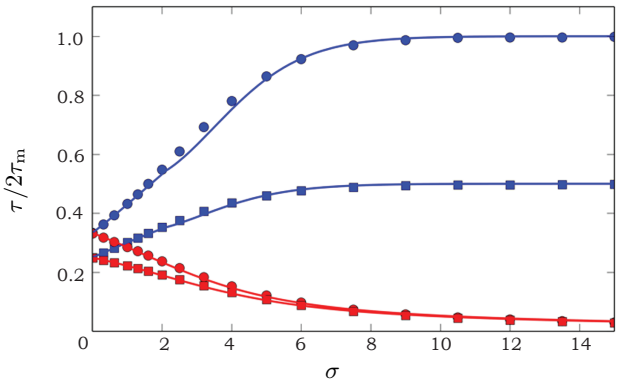

Fig. 11. Correlation decay times in the weak field limit ($\xi = 10^{-2}$) of magnetic moment components parallel (blue) and perpendicular (red) to the anisotropy axis of the particle. Numerical simulation was performed with $\epsilon = 0.5$ (circles) and $\epsilon = 1$ (squares). Lines represent the theoretical expressions [37].

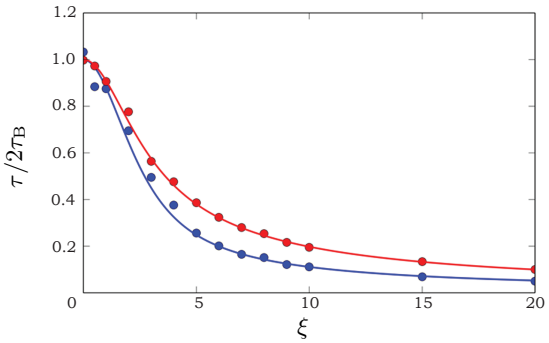

Fig. 12. Correlation decay times in the rigid dipole limit ($\sigma = 10^3$) of magnetic moment components parallel (blue) and perpendicular (red) to the external field. Numerical simulation (circles) is compared to theoretical expressions (lines) [38].

acteristic rotational diffusion times of the "yolk" and the "egg", respectively. In the limits of a weak field and a rigid dipole, the time correlation functions may be well approximated by single exponentials. The decay times of these exponentials are in good agreement with theoretical expressions, as shown in Figs. 11 and 12.

For an intermediate range of magnetic field strength and magnetic anisotropy, the time correlation functions should be approximated by sums of exponentials as follows:

$$\overline{\mu_{z\tau}\mu_{z0}} = \mu^2 \left(C_{z,0}^2 + \sum_k C_{z,k}\, \mathrm{e}^{-\tau/\tau_{z,k}} \right),$$

$$\overline{\mu_{x\tau}\mu_{x0}} = \overline{\mu_{y\tau}\mu_{y0}} = \mu^2 \sum_k C_{xy,k}\, \mathrm{e}^{-\tau/\tau_{xy,k}}.$$

Numerical simulation gives correct values for the mean-square fluctuation of μ_z, namely,

$$\sum_k C_{z,k} = 1 - 2\frac{L(\xi)}{\xi} - L^2(\xi),$$

where $L(\xi)$ is the Langevin function. Fig. 13 shows two decay times of $\mu_{z\tau}$, μ_{z0} at intermediate values of anisotropy and external field. They result from contri-

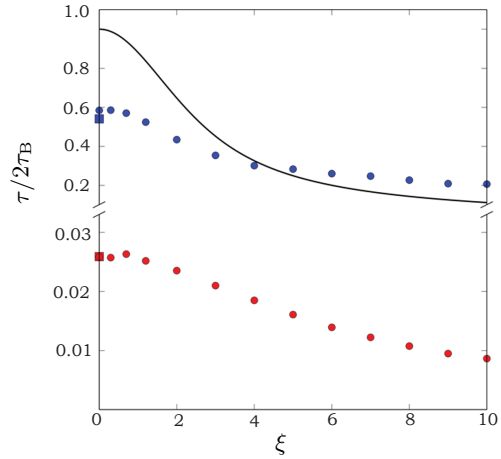

Fig. 13. Numerically computed decay times (circles) of $\mu_{z\tau}$, μ_{z0} with $\sigma = 5$, $\epsilon = 0.1$. As a comparison, the theoretical decay time of the rigid dipole is shown (line). Squares represent the theoretical decay times for the magnetic moment components parallel (blue) and perpendicular (red) to the anisotropy axis of the particle [37].

butions of the magnetic moment components parallel and perpendicular to the particles anisotropy axis, leading to a slow and a fast decay time, respectively.

As a result for the longitudinal ($T_1^{-1} = R_1 c$) and transversal ($T_2^{-1} = R_2 c$) coefficients of the relaxivity $R_{1,2}$ (c is the molar concentration of iron in the sample), we obtained [39]:

$$R_1 = A\left[6\,C_{z,0}^2\,j(i\omega_I\tau_{\mathrm{D}}) + 6\sum_k C_{z,k}\,j\left(i\omega_I\tau_{\mathrm{D}} + \frac{\tau_{\mathrm{D}}}{\tau_{z,k}}\right) + 14\sum_k C_{xy,k}\,j\left(i\omega_I\tau_{\mathrm{D}} + \frac{\tau_{\mathrm{D}}}{\tau_{xy,k}}\right)\right], \tag{1}$$

$$R_2 = \frac{R_1}{2} = A\left[4\,C_{z,0}^2 + 4\sum_k C_{z,k}\,j\left(\frac{\tau_{\mathrm{D}}}{\tau_{z,k}}\right) + 6\sum_k C_{xy,k}\,j\left(\frac{\tau_{\mathrm{D}}}{\tau_{xy,k}}\right)\right], \tag{2}$$

where

$$A = \frac{16\pi\gamma_I^2 M_{\mathrm{s}}^2 \rho M V_{\mathrm{m}}}{135 D R n_{\mathrm{Fe}}},$$

and

$$j(z) = \Re\mathrm{e}\left\{\frac{1 + \frac{1}{4}z^{1/2}}{1 + z^{1/2} + \frac{4}{9}z + \frac{1}{9}z^{3/2}}\right\},$$

and where γ_I is the proton gyromagnetic ratio, M_{s} the saturation magnetization of the particle, ρ the density of the particle, M the molar weight of mineral that constitute the particle, D the self-diffusion coefficient of water molecules, R the radius of the particle, n_{Fe} the number of magnetic atoms in the formula unit of the constituting material, and $\tau_{\mathrm{D}} = R^2/D$ is the characteristic diffusion time of the proton in the vicinity of the particle.

The model described by relations (1) and (2) was checked with existing experimental data. The relaxivity coefficient R_2 increases linearly with the size of the nanoparticle according to [40]. This result is in agreement with relation (2). It is known that the relaxivity of the nanoparticles R_1 exhibits maximum as a function of the external magnetic field strength. It flattens out with the increase of the particle size or magnetic anisotropy constant, as shown in [41] by comparison of

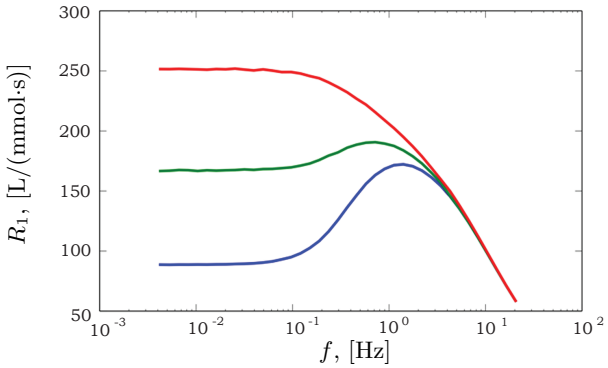

Fig. 14. Numerical simulation of R_1 with different magnetic anisotropy constants. $K = 10^3$ (blue line), $K = 5 \cdot 10^3$(green line) and $K = 10^4$(red line). Other parameters of the simulation are $\varepsilon = 0.0043$, core and hydrodynamic diameters of the particle $d_{\mathrm{c}} = d_{\mathrm{h}} = 20\,\mathrm{nm}$, $T = 312\,\mathrm{K}$, $M_{\mathrm{s}} = 300\,\mathrm{kA/m}$, $\eta = 6.7 \cdot 10^{-4}\,\mathrm{Pa{\cdot}s}$, $M = 0.23\,\mathrm{kg/mol}$, $\rho = 5.15\,\mathrm{g/cm^3}$, $n_{\mathrm{Fe}} = 3$.

the relaxivity data for maghemite and cobalt ferrite nanoparticles. Our numerical simulation confirms this behavior, as shown in Fig. 14. The verified model was applied to the experimental data.

Experimental data for various synthetic inorganic and biological samples are shown in Table 1. Numerical simulations were performed to compute relaxivities using the model and are shown in Table 2. The physical parameters of the particles, i.e. core diameters and field of saturation magnetization were chosen to reflect values obtained from the real particles. An exception was the hydrodynamic size of the particle that was kept close to the magnetic core size, with only a small (2.5 nm) non-magnetic layer. This characterizes the ability of water molecules to enter the non-magnetic coating layer. Use of the measured hydrodynamic size leads to modeled relaxivity values that are in disagreement with experimental values.

To demonstrate the effect of saturation magnetization Ms on relaxation parameters, various values were used in numerical simulation and the results are shown in Figs. 15 – 17. Other parameters were kept the same, as in Table 2, and $d_h = d_c + 5\,\text{nm}$. Both R_1 and R_2 increase with M_s, as expected by relations (1) and (2), but their ratio is invariant. In general, the numerical model predicts that at a constant external field (0.94 T) the most important physical parameters of the particles are their magnetic core size and saturation magnetization as these parameters change the relaxivities the most. Effects from other parameters are small or vanishing.

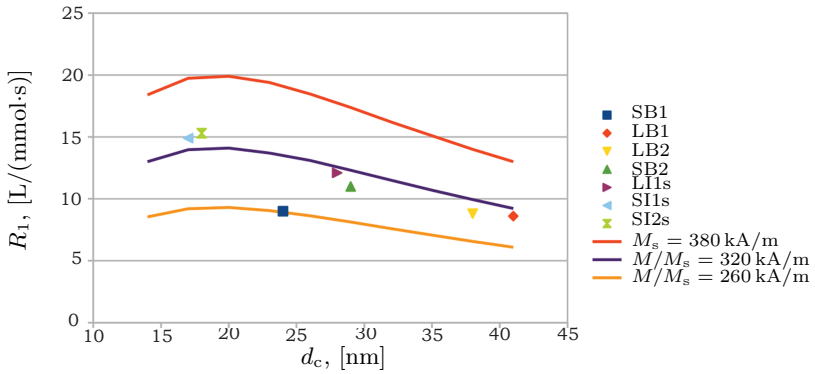

Fig. 15. Comparison of R_1 measured at 0.94 T (markers) with those computed numerically for various values of magnetization (lines).

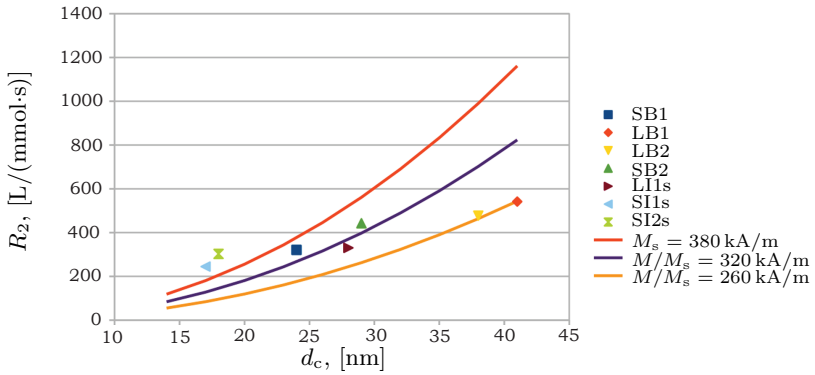

Fig. 16. Comparison of R_2 measured at 0.94 T (markers) with those computed numerically for various values of magnetization (lines).

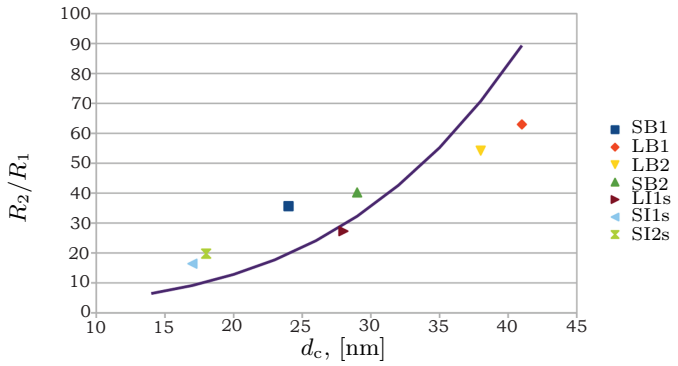

Fig. 17. Comparison of R_2/R_1 values measured at 0.94 T (markers) with those computed numerically (line).

Table 2. Results of numerical simulation. Common parameters: magnetite particles in water, anisotropy energy density $K = 10\,\mathrm{kJ/m^3}$, $B = 0.94\,\mathrm{T}$, $T = 39\,^\circ\mathrm{C}$. Here ε is the ratio between "inner" and "outer" viscosities of the nanoparticle [4].

Sample	d_c [nm]	d_h [nm]	M_s [kA/m]	ε	R_1 [L/mmol·s]	R_2 [L/mmol·s]	R_2/R_1
SB1	24	29	300	0.0024	11.9	234	19.7
LB1	41	46	300	0.0030	8.1	723	89.3
LB2	38	43	300	0.0029	8.7	617	70.9
SB2	29	34	300	0.0026	10.8	349	32.3
LI1s	28	33	357	0.0031	15.7	460	29.3
SI1s	17	22	358	0.0023	17.5	160	9.1
SI2s	18	23	329	0.0022	14.9	153	10.3

3. Conclusions. This multidisciplinary study shows that stable magnetic nanoparticles with a limited size distribution can be produced either biologically or synthetically, with particle size distributions being narrower for the biological samples. Small particles exhibit predominantly SP behavior, whereas the magnetic properties of samples consisting of larger particles show a combination of SP and SD behavior. Stabilization of the synthetic, inorganic particles prevents aggregation, so that small particles are almost exclusively SP in their magnetic properties.

Both types of particles, the biological as well as the synthetic ones, provide enhanced relaxation properties compared to the known MRI contrast agent Resovist. A significantly larger particle core diameter leads to a higher R_2 relaxivity. Combined with a low R_1 relaxivity, the R_1/R_2 relaxivity values of these particles are highly improved. Due to the insufficient colloidal stability of the large synthetic particles, only the small particles were investigated. These particles offer enhanced contrast properties with respect to Resovist but reduced contrast compared to the biological magnetosomes. A comparison to the MRI relaxivity that was measured for the particles with the simulated values shows the same trend in R_2/R_1 as a function of the particles size. Therefore, this model can aid further in exploring which physical properties of a material, such as core particle size, hydrodynamic diameter, or M_s, will lead to improved contrast properties. No enhanced toxicity was found for larger particles, while higher toxicity was measured for biological particles. Therefore, combining size effect, colloidal stability and low toxicity with

improvements in the stabilization of the synthetic particles, in particular, of those with the large core diameter, has the potential of providing particles with enhanced relaxation properties without problems associated with toxicity.

4. Materials and methods. We produced and analyzed 50 bacterial and 80 synthetic samples of magnetite nanoparticles. Procedures of the production of both biogenic and synthetic samples were continually refined in response to the results of sample characterization, in order to achieve the highest purity magnetite and the best performance of the particles as MRI contrast agents. We exemplify our findings on typical samples presented in Table 1.

4.1. Magnetite synthesis. Magnetite nanoparticles were synthesized by the modified co-precipitation method [9, 10]. Briefly, the system was controlled by a titration set-up (Metrohm, 776 Dosimat and 719 S Titrino). The iron was added as Fe^{II}/Fe^{III}-chloride solutions (1 M, $Fe^{II}/Fe^{III} = 1/2$) at a rate of 1 μl/min to a total volume of 10 ml. The pH and the temperature were kept constant during the process (pH = 9 ± 0.4 or 11 ± 0.1 with 1 M NaOH; temperature = $25 \pm 0.1\,^{\circ}$C). All solutions were degassed before using and the system was kept under a nitrogen atmosphere during the synthesis.

4.2. Stabilization of synthetic particles. The colloidally unstable particle dispersion was treated with an ultrasonic tip (Bandelin Sonoplus, duration = 30 s with 60% power) to reduce the size of large particle aggregates. Afterwards, the particle dispersion was mixed 1/1 (v/v) with a 10 wt% polymeric solution and a saturated solution of L-DOPA, respectively. The solution was shaken for 3 h (Thermomixer comfort, Eppendorf) and finally centrifuged (Biofuge pico, Heraeus) for 5 min at 4000 rpm. The resulting supernatant, containing the stabilized particles, was removed and analyzed in terms of the particle size (DLS) and iron content.

4.3. Magnetosome formation, isolation and preparation. For the formation of biogenic magnetite particles, *Magnetosprillum gryphiswaldense* wild-type and mutant strains (Table S1) were grown anaerobically at 25°C in a 30 L Biostat C fermentor (B. Braun Biotech International, Melsungen, Germany) using a modified flask standard medium [42]. Cells were harvested after 24 – 36 h by tangential flow filtration and centrifugation (9250 g, 15 min, 4 °C). Pelleted cells were resuspended and washed twice in an ice-cold wash buffer (20 mM Hepes, 5 mM EDTA, pH 7.4). Subsequently, cell pellets were stored at –20 °C until use. For magnetosome isolation, cells were resuspended in 50 mM Hepes, 1 mM EDTA, 0.1 mM PMSF, pH 7.4 (7 ml per g fresh weight) and disrupted by 3 passages through a Microfluidizer M110-L system equipped with a 100 μm HZ10 diamond interaction chamber. After removal of cell debris by centrifugation (1000 rpm, 10 min, 4 °C), the supernatant was subjected to magnetic separation, as described earlier [43]. The resulting enriched magnetosome suspension was applied on a 50% (w/w) sucrose cushion and centrifuged at 230 000 g at 4 °C for 2 h. Finally, the supernatant was removed, the pelleted magnetosomes were resuspended in 10 mM Hepes, 1 mM EDTA, pH 7.4 and subsequently stored under an inert nitrogen atmosphere at 4 °C in order to prevent oxidation.

4.4. X-ray diffraction. The particles were analyzed, as previously described [10, 44]. Briefly, the material was dried with an α-quartz standard [23] on a Kapton thin film and measured in transmission with a 100 μm beam at a wavelength $\lambda \approx 0.82656$ Å at the μ-Spot beam line of the BESSY II synchrotron radiation facility, Berlin [45]. The particle size was determined by Scherrer analysis, i.e. by fitting the (311) peak with a pseudo-Voigt function and after correcting for instrumental peak broadening [26].

4.5. Transmission Electron Microscopy. The nanoparticles were deposited from a suspension onto Cu transmission electron microscopy (TEM) grids covered with either lacey or continuous Formvar+carbon films. Bright-field and high-resolution (HRTEM) images, as well as selected-area electron diffraction (SAED) patterns were obtained using a JEOL 3010 transmission electron microscope operated at 300 kV accelerating voltage and equipped with a Gatan Imaging Filter for the acquisition of energy-filtered elemental maps. Images were recorded on a CCD camera. Additionally, bright-field images and SAED patterns were also recorded on imaging plates using a Philips CM20 TEM operated at 200 kV. For the processing and interpretation of data, we used the Digital Micrograph and SingleCrystal software.

4.6. Magnetic measurements. All magnetic measurements were made using a Princeton Measurements Corporation, Vibrating Sample Magnetometer (VSM; Micro-Mag Model 3900) at room temperature. Hysteresis loops were measured under a maximum applied field of 1 T with 100 ms averaging time and variable measurement spacing. FORC measurements were made by first saturating the sample with a positive applied field of 1 T and then ramping down the field to a reversal field (H_r), followed by measuring magnetization as the field increases from reversal field back to positive saturation. A series of 140 FORC with a field spacing of 2.4 mT was used for the analysis. FORC data were transformed into FORC diagrams using M. Winklhofer MATLAB code [46]. FORC diagrams were processed with a smoothing factor of 2.

4.7. Biocompatibility tests. The following various cell lines were used to determine IGC50 values of magnetic nanoparticles (MNPs): NIH3T3 (fibroblasts), MC3T3-E1 (osteoblasts) and RAW264.7 (macrophages). These cells were cultured in Dulbecco's modified eagles medium (DMEM) with 10% fetal bovine serum (FBS) and 50 μg/ml gentamycin. Cultures were performed under a humidified atmosphere at 37 °C and 5% CO_2. For experiments, the cells were seeded in DMEM with 2% FBS and 50 μg/ml gentamycin at a density of 2×10^4 cells $\times$ cm^{-2} in a 96-well plate. After 24 hours of cultivation, the culture medium was changed and inorganic samples or biological samples were added to the cells, followed by an incubation time of 72 hours. The IGC50 values were calculated from dose-response curves ranging from 0.005 to 2 mg/ml inorganic or biological samples $\times$ cm^{-2} according to Lee *et al.* by using nonlinear least-squares analysis [47]. For identifying IGC50 values, two different biochemical assays were used. First was the EZ4U assay (colorimetric MTT assay; Biomedica, Austria) which is based on the principle that living cells reduce uncoloured tetrazolium salts into intensely coloured formazan derivates that requires functional mitochondriae. Second was the CytoTox ONE Membrane Integrity assay (Promega) which measures lactate dehydrogenase (LDH) release that is based on the conversion of resazurin into resorufin. Because MTT and LDH assays are colorimetric assays, MNPs and BMGs were removed prior to the incubation with the assay substrates to prevent optical interference [48].

4.8. Relaxation times. The relaxation times of the magnetic nanoparticles were determined using a Bruker mq 40 contrast agent analyzer (0.94 T at 40 MHz). The relaxation times T_1 and T_2 in [ms] were measured at 39 °C using aqueous particle dispersions of 0.1, 0.25 and 0.5 mM iron, respectively. The relaxivities R_1 and R_2 in [L/(mmol·s)] were determined by applying the linear relationship of the reciprocal of the relaxation time $1/T_{1,2}$ in [s^{-1}] and the iron concentration c(Fe) in [mM]. Finally, the relaxivity $R_{1,2}$ was defined by the slope of the obtained linear equation.

4.9. DLS. Dynamic light scattering (DLS) was used to characterize the colloidal stable particles in terms of their size. The hydrodynamic diameter d_{h} was measured with a Submicron Particle Sizer Model 370 from Nicomp Particle Sizing Systems.

4.10. Iron concentration measurements. The iron content was measured using a UV/VIS phenanthroline assay. Briefly, hydrochloric acid was added to a defined volume of the particle suspension in order to dissolve the iron oxide particles. Afterwards the iron ions were reduced to Fe^{2+} by following complexation with 1,10-Phenathroline. The iron content was determined by using the linear relationship of absorbance and iron concentration (using calibration standards).

This multidisciplinary study shows that stable magnetic nanoparticles with a limited size distribution can be produced either biologically or synthetically, with particle size distributions being narrower for the biological samples. Small particles exhibit predominantly SP behavior, whereas the magnetic properties of samples consisting of larger particles show a combination of SP and SD behavior. Stabilization of the synthetic, inorganic particles prevents aggregation, so that small particles are almost exclusively SP in their magnetic properties.

Both types of particles, the biological as well as the synthetic ones, provide enhanced relaxation properties compared to the known MRI contrast agent Resovist. A significantly larger particle core diameter leads to a higher R_2 relaxivity. Combined with a low R_1 relaxivity, the R_2/R_1 relaxivity values of these particles are highly improved. Due to the insufficient colloidal stability of the large synthetic particles, only the small particles were investigated. These particles offer enhanced contrast properties with respect to Resovist but reduced contrast compared to the biological magnetosomes. A comparison to the MRI relaxivity that was measured for the particles with the simulated values shows the same trend in R_1/R_2 as a function of the particles size. Therefore, this model can aid further in exploring which physical properties of a material, such as core particle size, hydrodynamic diameter, or M_{s}, will lead to improved contrast properties. No enhanced toxicity was found for larger particles, while higher toxicity was measured for biological particles. Therefore, combining size effect, colloidal stability and low toxicity with improvements in the stabilization of the synthetic particles, in particular, of those with the large core diameter, has the potential of providing particles with enhanced relaxation properties without problems associated with toxicity.

Acknowledgements.
We thank H. Möhwald for the critical reading of the manuscript. This work was supported by the European Union (Project Bio2MaN4MRI No.245542). Financial support to DF from the European Research Council (Starting Grant MB2 No.256915) and from the Max Planck Society is acknowledged. We thank Chenghao Li and Stefan Siegel for technical assistance at the SPOT Beamline (BESSY Synchrotron, Berlin).

References

[1] L.K. Bogart, G. Pourroy, C.J. Murphy Nanoparticles for imaging, sensing, and therapeutic intervention. *ACS. Nano*, vol. 8 (2014), pp. 3107–3122.

[2] L.H. Reddy, J.L. Arias, J. Nicolas, P. Couvreur. Magnetic nanoparticles: design and characterization, toxicity and biocompatibility, pharmaceutical and biomedical applications. *Chem. Rev*, vol. 112 (2012), pp. 5818–5878.

[3] Z. Zhou, Z. Zhao, H. Zhang *et al.* Interplay between longitudinal and transverse contrasts in Fe_3O_4 nanoplates with (111) exposed surfaces. *ACS Nano*, vol. 8 (2014), pp. 7976–7985.

[4] T. Ahmad, H. Bae, I. Rhee *et al.* Particle size dependence of relaxivity for silica-coated iron oxide nanoparticles. *Curr. Appl. Phys*, vol. 12 (2012), pp. 969–974.

[5] S.H. Xuan, Y.X.J. Wang, J.C. Yu, K.C.F. Leung. Tuning the grain size and particle size of superparamagnetic Fe_3O_4 microparticles. *Chem. Mater*, vol. 21 (2009), pp. 5079–5087.

[6] S. Laurent, D. Forge, M. Port *et al.* Magnetic iron oxide nanoparticles: synthesis, stabilization, vectorization, physicochemical characterizations, and biological applications. *Chem. Rev*, vol. 108 (2008), pp. 2064–2110.

[7] D. Faivre, D. Schüler. Magnetotactic bacteria and magnetosomes. *Chem. Rev*, vol. 108 (2008), pp. 4875–4898.

[8] M.R. Lisy, A. Hartung, C. Lang *et al.* Fluorescent bacterial magnetic nanoparticles as bimodal contrast agents. *Invest. Radiol*, vol. 42 (2007), pp. 235–241.

[9] J. Baumgartner, A. Dey, P.H.H. Bomans *et al.* Nucleation and growth of magnetite from solution. *Nat. Mater*, vol. 12 (2013), pp. 310–314.

[10] J. Baumgartner, L. Bertinetti, M. Widdrat, A.M. Hirt, D. Faivre. Formation of magnetite nanoparticles at low temperature: from superparamagnetic to stable single domain particles. *Plos One*, vol. 8 (2013), pp. e57070.

[11] A. Scheffel, A. Gärdes, K. Grünberg, G. Wanner, D. Schüler. The major magnetosome proteins MamGFDC are not essential for magnetite biomineralization in *Magnetospirillum gryphiswaldense*, but regulate the size of magnetosome crystals. *J Bacteriol*, vol. 190 (2008), pp. 377–386.

[12] A. Lohsse, S. Ullrich, E. Katzmann *et al.* Functional analysis of the magnetosome island in *Magnetospirillum gryphiswaldense*: the mamAB Operon is sufficient for magnetite biomineralization. *Plos One*, vol. 6 (2011), pp. e25561.

[13] D. Murat, V. Falahati, L. Bertinetti *et al.* The magnetosome membrane protein, MmsF, is a major regulator of magnetite biomineralization in *Magnetospirillum gryphiswaldense* AMB-1. *Mol. Microbiol*, vol. 85 (2012), pp. 684–699.

[14] C. Carvallo, A.R. Muxworthy, D.J. Dunlop. First-order reversal curve (FORC) diagrams of magnetic mixtures: micromagnetic models and measurements. *Phys. Earth Planet Int*, vol. 154 (2006), pp. 308–322.

[15] A.R. Muxworthy, J.G. King, D. Heslop. Assessing the ability of first-order reversal curve (FORC) diagrams to unravel complex magnetic signals. *J. Geophys. Res*, vol. 110 (2005), pp. B11101, doi:11110.11029/12004 JB003195.

[16] C.R. Pike, A.P. Roberts, K.L. Verosub. Characterizing interactions in fine magnetic particle systems using first order reversal curves. *J. Appl. Phys*, vol. 85 (1999), pp. 6660–6667.

[17] A.P. Roberts, C.R. Pike, K.L. Verosub. First-order reversal curve diagrams: a new tool for characterizing the magnetic properties of natural samples. *J. Geophys. Res*, vol. 105 (2000), pp. 28461–28475.

[18] M. Kumari, M. Widdrat, E. Tompa *et al.* Distinguishing magnetic particle size of iron oxide nanoparticles with first-order reversal curves. *J. Appl. Phys*, vol. 116 (2014), pp. 124304.

[19] A. Javid, S. Ahmadian, A.A. Saboury, S.M. Kalantar, S. Rezaei-Zarchi. Chitosan-coated superparamagnetic iron oxide nanoparticles for doxorubicin delivery: synthesis and anticancer effect against human ovarian cancer cells. *Chem Biol. Drug Des*, vol. 82 (2013), pp. 296–306.

[20] A. Kroll, C. Dierker, C. Rommel *et al.* Cytotoxicity screening of 23 engineered nanomaterials using a test matrix of ten cell lines and three different assays. *Particle and Fibre Toxicology*, vol. 8 (2011).

[21] J. Peng, X. He, K. Wang *et al.* An antisense oligonucleotide carrier based on amino silica nanoparticles for antisense inhibition of cancer cells. Nanomed-Nanotechnol. *Biol. Med*, vol. 2 (2006), pp. 113–120.

[22] C.M. Sayes, K.L. Reed, D.B. Warheit. Assessing toxicity of fine and nanoparticles: comparing in vitro measurements to *in vivo* pulmonary toxicity profiles. *Toxicol. Sci*, vol. 97 (2007), pp. 163–180.

[23] S.M. Hussain, K.L. Hess, J.M. Gearhart, K.T. Geiss, J.J. Schlager. In vitro toxicity of nanoparticles in BRL 3A rat liver cells. *Toxicol. in Vitro*, vol. 19 (2005), pp. 975–983.

[24] T. Zhang, L. Qian, M. Tang *et al.* Evaluation on cytotoxicity and genotoxicity of the L-glutamic acid coated iron oxide nanoparticles. *J. Nanosci. Nanotechnol*, vol. 12 (2012), pp. 2866–2873.

[25] L.F. Gamarra, G.E.S. Brito, W.M. Pontuschka *et al.* Biocompatible superparamagnetic iron oxide nanoparticles used for contrast agents: a structural and magnetic study. *J. Magn. Magn. Mater*, vol. 289 (2005), pp. 439–441.

[26] L.X. Tiefenauer, A. Tschirky, G. Kühne, R.Y. Andres. In vivo evaluation of magnetite nanoparticles for use as a tumor contrast agent in MRI. *Magn. Res. Imaging*, vol. 14 (1996), pp. 391–402.

[27] A. Petri-Fink, B. Steitz, A. Finka, J. Salaklang, H. Hofmann. Effect of cell media on polymer coated superparamagnetic iron oxide nanoparticles (SPIONs): colloidal stability, cytotoxicity, and cellular uptake studies. *Eur. J. Pharma Biopharma*, vol. 68 (2008), pp. 129–137.

[28] S. Wagner, J. Schnorr, H. Pilgrimm, B. Hamm, M. Taupitz. Monomer-coated very small superparamagnetic iron oxide particles as contrast medium for magnetic resonance imaging: preclinical *in vivo* characterization. *Investigative Radiology*, vol. 37 (2002), pp. 167–177.

[29] E. Amstad, T. Gillich, I. Bilecka, M. Textor, E. Reimhult. Ultrastable iron oxide nanoparticle colloidal suspensions using dispersants with catechol-derived anchor groups. *Nano Lett*, vol. 9 (2009), pp. 4042–4048.

[30] F. Roohi, J. Lohrke, A. Ide, G. Schuetz, K. Dassler. Studying the effect of particle size and coating type on the blood kinetics of superparamagnetic iron oxide nanoparticles. *Int. J. Nanomed.*, vol. 7 (2012), pp. 4447–4458.

[31] D. Pouliquen, J.J. Lejeune, R. Perdrisot, A. Ermias, P. Jallet. Iron-oxide nanoparticles for use as an MRI contrast agent – pharmacokinetics and metabolism. *Magn. Reson. Imag.*, vol. 9 (1991), pp. 275–283.

[32] R. Weissleder, M. Nahrendorf, M.J. Pittet. Imaging macrophages with nanoparticles. *Nat. Mater*, vol. 13 (2014), pp. 125–138.

[33] Y.-X.J. Wang, S.M. Hussain, G.P. Krestin. Superparamagnetic iron oxide contrast agents: physicochemical characteristics and applications in MR imaging. *Europ. Radiol.*, vol. 11 (2001), pp. 2319–2331.

[34] C. Chouly, D. Pouliquen, I. Lucet, J.J. Jeune, P. Jallet. Development of superparamagnetic nanoparticles for MRI: effect of particle size, charge and surface nature on biodistribution. *J. Microencapsul*, vol. 49 (201013 (1996)), pp. 245–255.

[35] Y. Ayant, E. Belorizky, J. Alizon, J. Gallice. Calculation of special densities for relaxation resulting from random modecular translational modulation of magnetic dipolar coupling in liquids. *J. Phys.*, vol. 36 (1975), pp. 991–1004.

[36] M.I. Shliomis, V.I. Stepanov. Rotational viscosity of magnetic fluids – contribution of the Brownian and Neel relaxational process. *J. Magn. Magn. Mater.*, vol. 122 (1993), pp. 196–199.

[37] M.I. Shliomis, V.I. Stepanov. Frequency-dependence and long-time relaxation of the susceptibility of the magnetic fluids. *J. Magn. Magn. Mater.*, vol. 122 (1993), pp. 176–181.

[38] Y.L. Raikher, M.I. Shliomis. The effective-field method in the operational kinetics of magnetic fluids and liquid crystals. *Relaxation Phenomena in Condensed Matter* (W. Coffey (editor), New York: John Wiley & Sons Inc., 1994), pp. 595–751.

[39] R. Taukulis, A. Cebers. Coupled stochastic dynamics of magnetic moment and anisotropy axis of a magnetic nanoparticle. *Phys. Rev. E*, vol. 86 (2012).

[40] Q.L. Vuong, J.F. Berret, J. Fresnais, Y. Gossuin, O. Sandre. A universal scaling law to predict the efficiency of magnetic nanoparticles as MRI T_2-contrast agents. *Adv. Health Mater*, vol. 1 (2012), pp. 502–512.

[41] M. Levy, F. Gazeau, C. Wilhelm *et al.* Revisiting MRI contrast properties of nanoparticles: beyond the superparamagnetic regime. *J. Phys. Chem. C*, vol. 117 (2013), pp. 15369–15374.

[42] R. Uebe, B. Voigt, T. Schweder *et al.* Deletion of a *fur-like gene* affects iron homeostasis and magnetosome formation in *Magnetospirillum gryphiswaldense*. *J. Bacteriol*, vol. 192 (2010), pp. 4192–4204.

[43] C. Lang, D. Schüler. Expression of green fluorescent protein fused to magnetosome proteins in microaerophilic magnetotactic bacteria. *Appl. Environ. Microbiol*, vol. 74 (2008), pp. 4944–4953.

[44] A. Fischer, M. Schmitz, B. Aichmayer, P. Fratzl, D. Faivre. Structural purity of magnetite nanoparticles in magnetotactic bacteria. *J. R. Soc. Interface*, vol. 8 (2011), pp. 1011–1018.

[45] O. Paris, C.H. Li, S. Siegel *et al.* A new experimental station for simultaneous X-ray microbeam scanning for small- and wide-angle scattering and fluorescence at BESSY II. *J. Appl. Cryst*, vol. 40 (2007), pp. S466–S470.

[46] M. Winklhofer, G.T. Zimanyi. Extracting the intrinsic switching field distribution in perpendicular media: a comparative analysis. *J. Appl. Phys.*, vol. 99 (2006).

[47] J.K. Lee, D.B. Kim, J.I. Kim, P.Y. Kim. In vitro cytotoxicity tests on cultured human skin fibroblasts to predict skin irritation potential of surfactants. *Toxicol*, vol. 14 (2000), pp. 345–349.

[48] A. Kroll, M.H. Pillukat, D. Hahn, J. Schnekenburger. Current in vitro methods in nanoparticle risk assessment: limitations and challenges. *Eur. J. Pharmaceutics Biopharmaceutics*, vol. 72 (2009), pp. 370–377.

Supplementary Information.

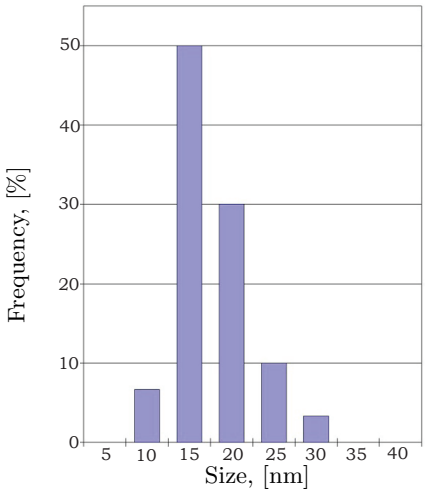

Fig. 18. Size distribution of particles in SI1 as measured from TEM images.

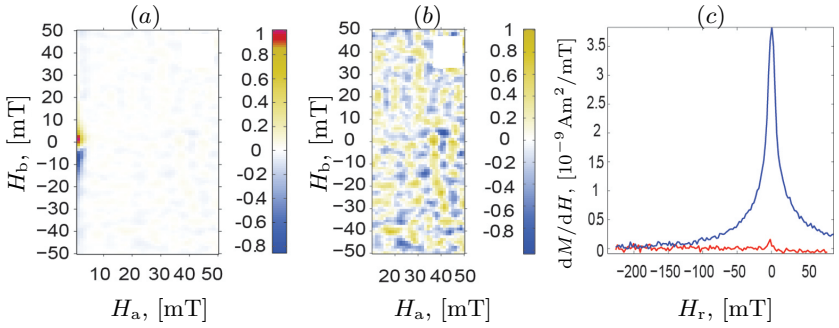

Fig. 19. (*a*) FORC diagram; (*b*) FORC diagram suppressing coercivity < 10 mT; and (*c*) derivatives of the magnetic moment showing reversible (blue) and irreversible (red) components of magnetization for the synthetic inorganic sample SI1s.

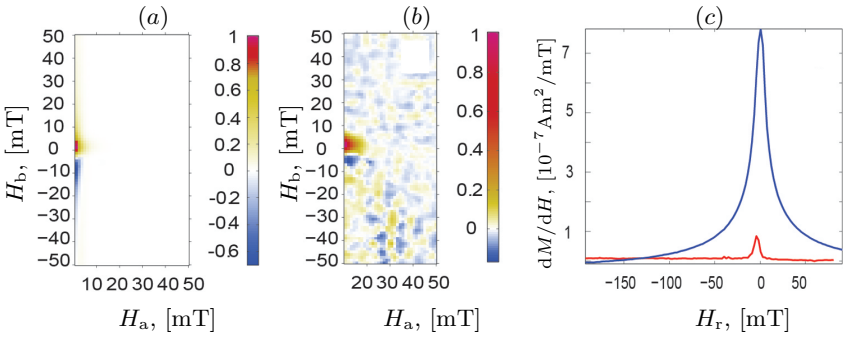

Fig. 20. (*a*) FORC diagram; (*b*) FORC diagram suppressing coercivity < 10 mT; and (*c*) derivatives of the magnetic moment showing reversible (blue) and irreversible (red) components of magnetization for Resovist.

Table 3. Bacterial strains used in this study.

Sample identifier	Strain	Important feature(s)	Reference
SB1	M. gryphiswaldense $\Delta F3D$	R3/S1 with deletion of all $mamF/mmsF$	Suppl. Ref. 1
LB1	M. gryphiswaldense $\Delta mms48$	R3/S1 $\Delta mms48$	Suppl. Ref. 2
LB2	M. gryphiswaldense R3/S1	Wildtype, but Rif^r Sm^r	Suppl. Ref. 3
SB2	M. gryphiswaldense $\Delta Fe4$	R3/S1 with mutations in iron uptake genes	Suppl. Ref. 1
LB3	M. gryphiswaldense $\Delta A11$	R3/S1 $\Delta mamGFDC$ and $\Delta mamXY operon$	Suppl. Ref. 4

Supplementary References

[1] M. Kumari, M. Widdrat, E. Tompa, R. Uebe, D. Schüler, M. Pósfai, D. Faivre, and A.M. Hirt. Distinguishing magnetic particle size of iron oxide nanoparticles with FORC analysis. *J. Appl. Phys.*, vol. 116 (2014), p. 124304.

[2] A. Lohsse, S. Borg, O. Raschdorf, I. Kolinko, E. Tompa, M. Posfai, D. Faivre, J. Baumgartner and D. Schüler. Genetic dissection of the

mamAB and mms6 operons reveals a gene set essential for magnetosome biogenesis in *Magnetospirillum gryphiswaldense*. *J. Bacteriol.*, vol. 196 (2014), pp. 2658–2669.

[3] D. Schultheiss, R. Handrick, D. Jendrossek, M. Hanzlik, D. Schüler. The presumptive magnetosome protein Mms16 is a poly(3-hydroxybutyrate) granule-bound protein (phasin) in *Magnetospirillum gryphiswaldense*. *J. Bacteriol.*, vol. 187 (2005), pp. 2416–2425.

[4] A. Lohsse, S. Ullrich, E. Katzmann, S. Borg, G. Wanner, M. Richter, B. Voigt, T. Schweder and D. Schüler. Functional analysis of the magnetosome island in *Magnetospirillum gryphiswaldense*: The mamAB operon is sufficient for magnetite biomineralization. *PloS One*, vol. 6 (2011), no. 10, p. e25561.

Received 02.09.2015